



ACADEMIE
DES SCIENCES
INSTITUT DE FRANCE
1666

Comptes Rendus

Mécanique

Gaëtan Boissonneau, Andréa Tommasi, Fabrice Barou, Marco Antonio Lopez-Sánchez and Maurine Montagnat

Supplementary Material: Dynamic recrystallization and mechanical behavior of Mg alloy AZ31: Constraints from tensile tests with in-situ EBSD analysis

Supplementary material to the article available at
<https://doi.org/10.5802/crmeca.267>

This article is licensed under the
CREATIVE COMMONS ATTRIBUTION 4.0 INTERNATIONAL LICENSE.
<http://creativecommons.org/licenses/by/4.0/>



The Comptes Rendus. Mécanique are a member of the
Mersenne Center for open scientific publishing
www.centre-mersenne.org — e-ISSN : 1873-7234



Supplementary material / Document complémentaire

Supplementary Material: Dynamic recrystallization and mechanical behavior of Mg alloy AZ31: Constraints from tensile tests with in-situ EBSD analysis

Gaëtan Boissonneau^{®,a}, Andréa Tommasi^{®,a}, Fabrice Barou^{®,a}, Marco Antonio Lopez-Sánchez^{®,b} and Maurine Montagnat^{®,c}

^a Geosciences Montpellier, CNRS, Université de Montpellier, France

^b Departamento de Geología, Universidad de Oviedo, Oviedo, Spain.

^c Univ. Grenoble Alpes, CNRS, IRD, G-INP, IGE, Grenoble, France

E-mails: gaetan.boissonneau@umontpellier.fr (G.Boissonneau),
andrea.tommasi@umontpellier.fr (A.Tommasi), fabrice.barou@umontpellier.fr
(F.Barou), lopezmarco@uniovi.es (M.A.Lopez-Sánchez),
maurine.montagnat@univ-grenoble-alpes.fr (M.Montagnat)

Manuscript received 13 June 2024, revised 28 August 2024, accepted 5 September 2024.

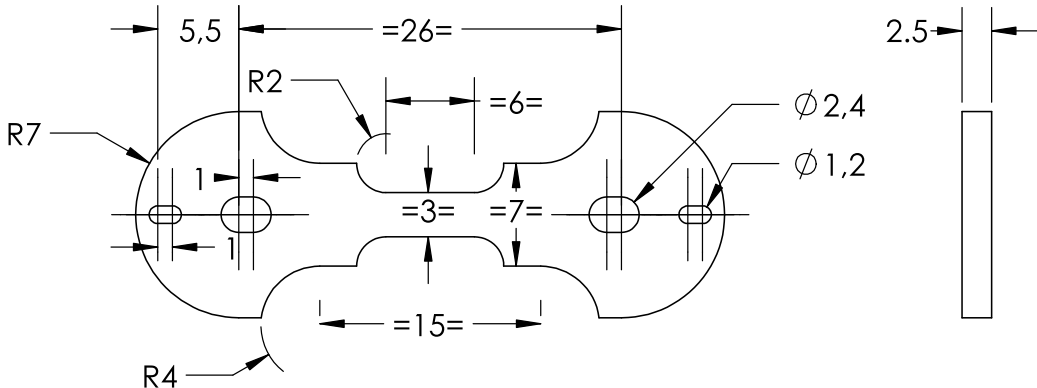


Figure S1. In-situ tensile test initial sample shape and dimensions (mm).

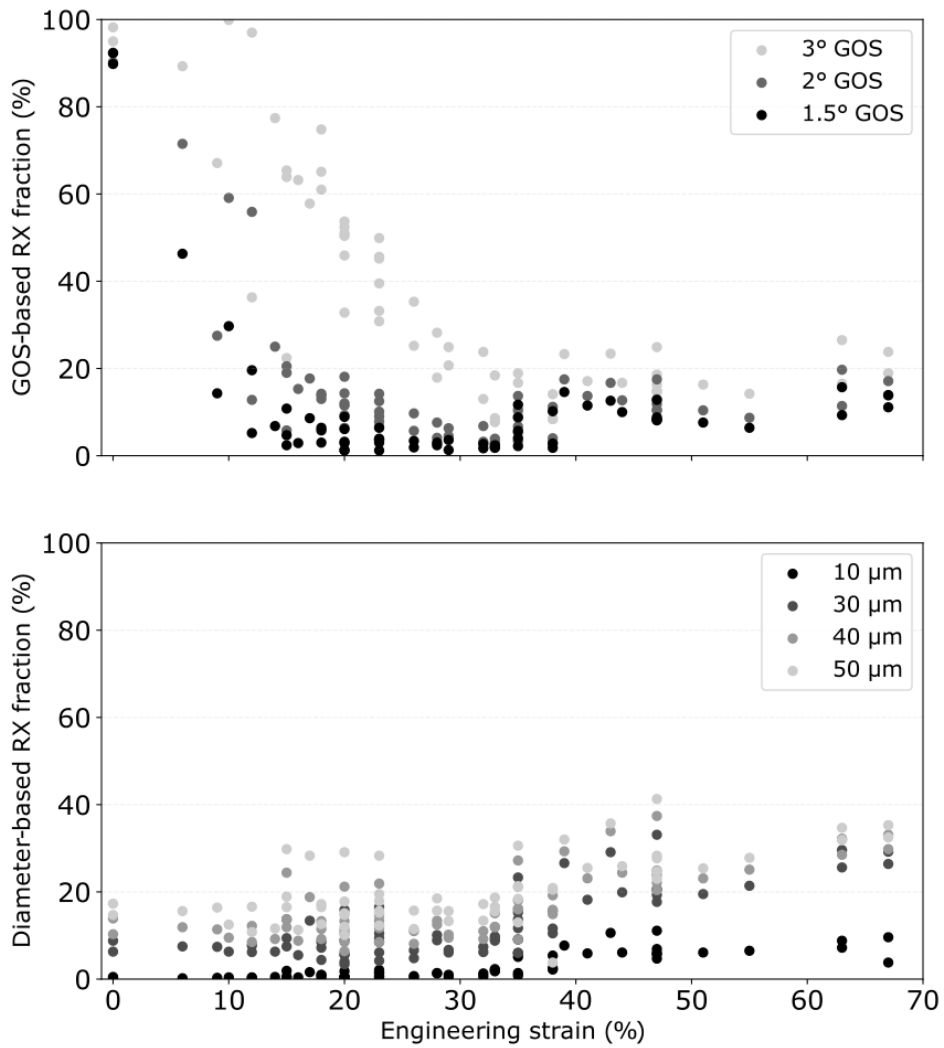


Figure S2. Recrystallized fraction estimated with various absolute values for both the GOS threshold (upper) and grain equivalent diameter threshold (lower).

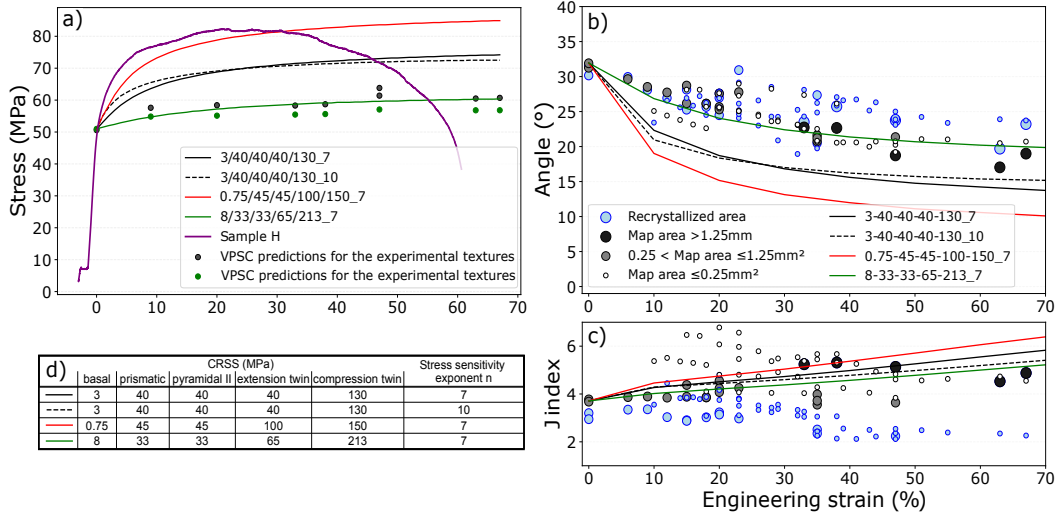


Figure S3. Comparison between the experimental results and predictions of VPSC simulations performed with various CRSS settings (cf. Table S3.d.). (a) Mechanical responses predicted using VPSC with the different sets of parameters for : (1) monotonic uniaxial tension experiments with as the initial texture that of the starting experimental material (full lines); (2) one-step predictions for the textures measured post mortem at different finite strains (dots), the color of the dots indicate the CRSS and stress exponent used in the simulation (cf. graphical legend).; The mechanical data for sample H is presented by the purple line. (b) Orientation of the texture, defined by the angle between the normal to the $\langle c \rangle$ axis girdle and the tension direction, predicted in the different simulations and observed in the experiments at different strains. (c) Texture strength, defined by the J-index. Symbols in white, gray, and black correspond to full orientation data (bulk texture), considering one orientation per measurement point. Coarser symbols mark data from larger, post mortem maps. The texture of the recrystallized fraction identified using a $20\ \mu\text{m}$ threshold in each map is represented by blue symbols; as for the full orientation data, the symbol sizes are proportional to the area of the map. (d) Slip and twin systems data used in the different simulations.

To evaluate the effect of viscoplastic anisotropy on the VPSC predictions, simulations were run with different CRSS and stress sensitivity values. The reference model has parameters adjusted to fit experimental data obtained at similar conditions to those in the present experiments. It has a factor 13 contrast between the CRSS of the basal and the prismatic or pyramidal systems. The other models have CRSS sets leading to significantly higher (a factor 60 contrast) and lower (a factor 4 contrast) viscoplastic anisotropies. In these additional simulations, the CRSS for the different slip systems were adjusted so that a similar S11 tensional stress was predicted for the starting material texture. We also tested, for the reference CRSS set, the effect of a higher stress exponent.

In all simulations, we used a normalization factor of 1. Boundary conditions are set as to mimic the experimental ones, with an imposed fixed rate extension in the direction 1 and null normal stresses in directions 2 and 3. Shear velocity gradients were null. Hardening was not considered in the simulations so that we could isolate, by comparing the predicted stresses for

the experimental textures to those for the textures predicted by a monotonic axial tension testing at the same strains, the effect of DRX on the geometrical hardening/softening.

Analysis of the results show that by reducing the viscoplastic anisotropy one better reproduces the experimental observations. The simulations with a low viscoplastic anisotropy presented do fit the experimentally observed texture evolution. However, such low CRSS contrasts are only expected to be observed at much higher temperatures ($>350^{\circ}\text{C}$) than the 250°C used in our experiments, as the viscoplastic anisotropy of AZ31 decreases with increasing temperature (Chapuis & Liu 2018, Zhang et al. 2021). Moreover, to be able to also reproduce the mechanical results of our experiments, one has to assume a rather high CRSS for the basal system. The reference VPSC simulation, which uses exactly the CRSS proposed by Chapuis & Liu (2018) to simulate deformation at 250°C (3-40-40-40-130 MPa), reproduces correctly the 50 MPa of tensional stress observed at the beginning of the viscoplastic deformation. However, if a lower viscoplastic anisotropy is considered, CRSS values of 8-33-33-65-213 MPa have to be used to obtain similar stresses for the initial texture, what is a much higher CRSS for the basal than usually described in the literature (cf. Chapuis & Liu 2018, Zhang et al. 2021 and references therein). The simulations presented in Figure S3 show indeed that the lower the assumed viscoplastic anisotropy, the higher is the CRSS of the basal system needed to adjust the mechanical behavior at the start of the viscoplastic deformation in the experiments. Yet an increase in temperature should both decrease viscoplastic anisotropy and the CRSS for basal glide.

The fact that simulations with lower viscoplastic anisotropy better fit the experimental observations may, nevertheless, corroborate the assumption that an essential role of DRX is to resolve viscoplastic strain incompatibility that arises between differently oriented grains in highly anisotropic polycrystals.

Table T1. Parameters of the EBSD maps.

Sample	Engin.	Working	Acc.	Acquisiton	xCells	yCells	Step	Frame	Index.	Extension	Compression
	Strain	Distance	Voltage	Temperature	px	px	μm	Averag-	Rate	twin fraction	twin fraction
%	mm	kV	°C					%	%	%	%
C	33	24.9	20	20	2546	1394	1	1	95	1.032	0.308
D	38	24.9	20	20	2528	1383	1	1	94	0.795	0.313
F	47	24.9	20	20	2561	1398	1	2	93	0.225	0.168
H	63	25	20	20	5658	1571	1	2	86	5.427	0.105
X	67	25	20	20	6580	1581	1	2	80	0.120	0.152
X	0	29.1	20	150	403	327	2	2	98	4.151	0.049
X	6	29	20	250	404	321	2	2	94	0.914	0.317
X	9	29.2	20	250	403	319	2	2	91	1.128	0.366
X	12	29.2	20	250	403	327	2	2	93	1.545	0.327
X	15	29.4	20	250	403	327	2	2	90	1.267	0.323
X	35	29.7	20	250	403	327	2	2	70	0.643	0.230
C	18	30	20	20	806	655	1	1	92	0.662	0.303
D	15	30.2	15	20	403	327	2	1	86	5.520	0.215
Y	20	30.3	15	20	403	327	2	1	86	0.238	0.214
Y	0	24.9	15	20	604	491	2	2	94	0.172	0.607
F	35	30.6	20	20	806	655	1	1	79	0.300	0.417
G	20	30.1	20	20	806	655	1	2	95	0.852	0.266
X	47	31.3	20	20	537	436	1.5	2	85	2.628	0.160
D	23	30.7	20	20	537	436	1.5	2	94	0.597	0.332
C	10	30.1	15	20	483	393	1	1	96	9.835	0.072
C	12	30.1	15	250	483	393	1	1	91	1.919	0.173
C	14	30.2	15	250	483	393	1	2	93	1.887	0.207
C	16	30.2	15	250	483	393	1	2	89	1.606	0.201
C	18	30.2	15	250	483	393	1	2	84	1.45	0.212
C	18	30	20	150	483	393	1	2	95	1.489	0.344
C	23	30.1	20	150	483	393	1	2	93	0.513	0.429
C	28	30.2	20	150	483	393	1	3	91	0.312	0.369
C	33	30.5	20	150	483	393	1	4	90	0.338	0.391
D	15	30.2	15	20	711	484	0.5	1	83	0.974	0.162
D	17	30.3	15	250	711	480	0.5	2	82	0.281	0.281
D	20	30.4	15	250	711	480	0.5	2	76	0.000	0.432
D	23	30.4	15	250	711	470	0.5	2	65	0.142	0.247
D	20	30.4	15	250	403	327	2	1	71	1.284	0.300
D	23	30.6	20	20	483	393	1	2	94	0.236	0.217
D	28	30.6	20	150	483	393	1	2	90	0.104	0.173
D	33	30.7	20	150	483	393	1	3	90	0.069	0.500
D	38	30.8	20	150	483	393	1	4	89	0.088	0.398
Y	20	30.3	15	20	483	393	1	1	84	0.240	0.190
Y	23	30.4	15	250	483	393	1	2	80	0.105	0.157
Y	26	30.5	15	250	483	393	1	3	81	0.214	0.155
Y	29	30.6	15	250	483	393	1	3	77	0.139	0.225
Y	32	30.6	15	20	483	393	1	3	77	0.156	0.371
F	35	30.6	20	20	483	393	1	2	87	0.281	0.107
F	39	30.6	20	150	483	393	1	3	81	0.255	0.058
F	43	30.8	20	150	483	393	1	3	85	0.442	0.093
F	47	30.8	20	150	483	393	1	4	82	0.329	0.109
X	35	30.4	17	20	483	393	1	2	88	2.338	0.132
X	38	30.3	17	250	483	393	1	2	82	2.114	0.164
X	41	30.4	17	250	483	393	1	3	86	1.943	0.093
X	44	30.5	17	250	486	423	1	4	84	1.548	0.057
X	47	30.6	17	20	967	786	0.5	4	87	1.602	0.062
X	47	31.3	20	20	483	393	1	2	93	0.690	0.241
X	51	31.3	20	150	483	393	1	2	95	0.711	0.244
X	55	31.4	20	150	483	393	1	2	92	0.774	0.299
X	63	31.7	20	150	483	393	1	3	87	0.568	0.250
X	67	31.6	20	20	483	393	1	4	85	0.444	0.147
G	20	30	20	250	483	393	1	2	95	0.469	0.399
G	23	30	20	250	483	393	1	2	94	0.594	0.352
G	26	30	20	250	483	393	1	2	93	0.830	0.435
G	29	30.1	20	250	483	393	1	3	95	1.001	0.352
G	32	30.2	20	250	483	393	1	3	93	0.612	0.306
G	35	30.2	20	250	483	393	1	4	93	0.655	0.334